A quantitative criterion for predicting solid-state disordering during biaxial, high strain rate deformation

Michael F Becker^{1,2,*} and Desiderio Kovar^{1,3} and Desiderio Kovar^{1,3} ■

- ¹ Materials Science and Engineering Program and Center for Additive Manufacturing and Design Innovation, The University of Texas at Austin, Austin, TX 78712, United States of America
- ² Department of Electrical and Computer Engineering, The University of Texas at Austin, Austin, TX 78712, United States of America
- ³ Department of Mechanical Engineering, The University of Texas at Austin, Austin, TX 78712, United States of America

E-mail: mfbecker@austin.utexas.edu

Received 14 September 2021, revised 11 November 2021 Accepted for publication 24 November 2021 Published 10 December 2021



Abstract

A criterion to predict the onset of disordering under biaxial loading based on a critical potential energy per atom was studied. In contrast to previous theories for disordering, this criterion incorporates the effects of strain rate and strain state. The strain state (or stress state) is defined by the combination of strain (or stress) magnitudes and directions that are applied to each sample during the simulation. The validity of this criterion was studied using molecular dynamic (MD) simulations of Ag conducted over a wide range of biaxial strain rates, strain configurations, and crystal orientations with respect to the applied stress state. Biaxial strains were applied in two different planes, $(11\overline{2})$ and (001) in eight directions in each plane. Results showed that, when larger strain rates were applied, there was a transition from plastic deformation driven by the nucleation and propagation of dislocations to disordering and viscous flow. Although the critical strain rate to initiate disorder was found to vary in the range of $\dot{\varepsilon} = 1 \times 1$ 10^{11} s^{-1} to $\dot{\varepsilon} = 4 \times 10^{11} \text{ s}^{-1}$, a consistent minimum PE/atom of -2.7 eV was observed over a broad range of strain states and for both crystallographic orientations that were studied. This indicates that the critical PE/atom is a material property that can be used to predict the onset of disordering under biaxial loading. Further, the results showed that this criterion can be applied successfully even when non-uninform strain states arise in the crystal.

^{*}Author to whom any correspondence should be addressed.

Keywords: high strain rate deformation, disorder transition in crystalline metals, plasticity in crystalline metals, molecular dynamics

(Some figures may appear in colour only in the online journal)

1. Introduction

The study of the disordering of solids has seen renewed interest since the observation of the solid-state disordering transition in molecular dynamic (MD) simulations of nano-sized solid materials deformed at high strain rates [1]. Both simulation and experimental results have shown that fcc metals [2–5] and ceramics [6–8] will disorder under loading at sufficiently high strain rates and strains. To understand this disorder transition, previous models for solid-state disordering were reviewed and found to be inadequate to predict a strain rate or strain dependence for initiating disordering under uniaxial loading [9]. Consequently, a new model was proposed based on a critical potential energy per atom (PE/atom) being a necessary criterion for solid-state disordering. In this paper, we will briefly review the models which have been proposed for disordering, including one which was shown to apply for disordering at high uniaxial strain rates. Our main objective is to show that this physics-based criterion for disordering for uniaxial loading can also be applied to biaxial loading. We suggest that biaxial strain occurs in several situations of practical interest where the geometry precludes the use of uniaxial strain analysis.

Previous models for predicting solid-state disordering were based on thermodynamic criteria with a large emphasis on atomic displacements. One model that successfully incorporated the varied disorder conditions of previous models was the modified Lindemann criterion [10, 11]. It incorporated the original Lindemann criterion via vibrational instability as measured by RMS atomic displacements [12]. It also included static atomic displacements, which could for example be due to strain or interstitials. A critical displacement for disordering was defined as an RMS sum of the various displacement contributions. It was shown that this model does not account for variation in the disorder criterion as a function of either strain rate or stress condition (strain geometry), two factors which have been shown to influence disordering [9]. An alternative criterion to predict disordering was proposed based a critical PE/atom for disordering that accounts for the influence of strain rate.

This disorder criterion predicts that when a critical PE/atom threshold is exceeded, and the strain rate is sufficiently large, atomic disordering will occur. These MD studies of uniaxial strain of fcc metals found critical thresholds for disordering of -2.70 eV atom⁻¹ for Ag and -3.62 eV atom⁻¹ for Au. At lower strain rates, dislocations formed fast enough to dissipate energy so that the PE/atom never reached the critical value and disordering did not occur. At higher strain rates, the inability of dislocation formation to dissipate energy sufficiently rapidly resulted in the critical PE/atom being exceeded and disordering ensued. The minimum strain rate required for disordering was found to be between 5 and 20% ps⁻¹ (5 \times 10¹⁰ s⁻¹ to 2×10^{11} s⁻¹), depending on crystal orientation, whereas the critical PE/atom did not vary. It was also shown that the critical PE/atom is easily estimated by doing a single equilibrium MD simulation at the crystal's melting point and measuring the average PE/atom at melt. A key observation was that PE/atom included all the aspects of atomic positions (both static and dynamic) of the previous models, but it also included rate dependent effects since the PE/atom and energy balance within the material could be affected by various energy dissipation mechanisms. Dissipation by the nucleation and motion of defects is affected by the stress state. Thus, strain rate can affect energy balance and PE/atom. In summary, the wide range of driving

Table 1. Strain directions and strain rates (in % of the base rate) that were applied at each strain angle along the x and y directions. The absolute strain rate component is computed by multiplying the % of the base rate by one of the five selected base strain rates.

	$\dot{arepsilon}_{\chi}$	$\dot{arepsilon}_y$	
Direction in (112) Direction in (001)	⟨111⟩ ⟨100⟩	⟨110⟩ ⟨010⟩	Strain angle
	-100%	0%	180°
	-100%	100%	135°
	0%	100%	90°
	100%	100%	45°
	100%	0%	0°
	100%	-100%	-45°
	0%	-100%	-90°
	-100%	-100%	−135°

forces that affect disordering all play a role in determining the PE/atom and whether a material will reach the critical disordering threshold.

Another factor that could influence the criterion for disordering is the stress state, since competing energy dissipation mechanisms such as the initiation of dislocations are stress state dependent. Thus, to test the general applicability of a criterion to predict disordering based on PE/atom, it is necessary to study the influence of the applied strain or stress state. In this paper, we first describe the geometry for applying biaxial strain in a wide variety of strain states to the Ag samples in the MD simulations. Then the details of the MD simulations are given. The first results are a complete display of parameters for two strain states which show prototypical behavior: first at a strain rate below the threshold for disorder where defect activity is observed, and then above the disorder threshold where deformation occurs by atomic disordering followed by viscous flow. The atomic configurations are followed for each case through the various transformations. Lastly, all the various stress states are simulated and analyzed. The onset strains for the transformation of the atomic configuration are given as a function of the strain state. The PE/atom is measured as a function of strain, strain rate, and strain state. These results are compared against the hypothesized criterion for disordering. An anomalous case is described that is found to be a case of inhomogeneous strain that obeys the criterion locally, and it suggests future application of the hypothesized disorder criterion to inhomogeneous strain states.

2. Procedures

MD simulations were performed over a range of biaxial strain rates using Ag as a prototypical material to study its disordering behavior. The influence of strain rate, strain state, and crystallographic orientations of the crystal relative to the applied biaxial strain directions were studied. Strains were applied to the faces of a cube-shaped, single-crystal bar at a constant engineering strain rate. The strain state was varied by controlling the direction of the applied strain rate in eight different combinations in the plane-direction pairs: $(11\overline{2})$ [111], $(11\overline{2})$ [1 $\overline{10}$], (001) [100], and (001) [010], as shown in table 1. These combinations of strain rate magnitudes are denoted by the angle of the vector sum of the orthogonal +x and +y applied strain components and define the *strain angle*. This is illustrated in figures 1(a)–(d). For strain angles of -45° (strain magnitudes in the +x direction = strain magnitude in the -y direction) to 90°

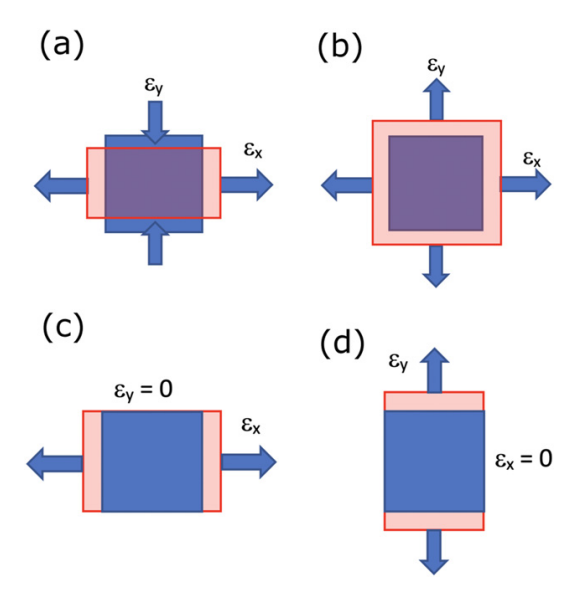


Figure 1. Schematics showing original bars (blue) and bars after deformation (red) to illustrate deformations when (a) positive tensile strain is applied in the x direction and an equal and opposite compressive strain is applied in the y direction, strain angle $= -45^\circ$; (b) equibiaxial tensile strain is applied in the x and y directions, strain angle $= 45^\circ$; (c) tensile strain is applied only in the x direction, strain angle $= 0^\circ$; (d) tensile strain sapplied only in the y direction while the x direction strain is fixed at zero, strain angle $= 90^\circ$. There were no applied strains in the z direction (out of the plane of the page), but the specimen was allowed to expand or contract freely in this direction.

(strain magnitudes in the +y direction and strain fixed at zero in the x direction). Taking the opposite values of the strain components for each of these cases results in four more strain angles, 135° , -135° , 180° , and -90° respectively. Note that a strain rate component of 0% denotes a plane strain condition where the strain in this direction is *fixed to zero* in that direction.

Strain rates were selected that span from relatively low strain rates where permanent deformation resulted from nucleation and then glide of dislocations to relatively high strain rates where permanent deformation resulted from atomic disordering, followed by viscous flow. These base strain rates were 1×10^9 , 1×10^{10} , 1×10^{11} , 4×10^{11} , and 4×10^{12} s⁻¹ (0.1 to 400 ps^{-1}). The strain rates are presented as a percentage of the base rates in table 1. For each simulation, strain components were applied at the selected engineering strain rate up until the strain magnitude was equal to 0.30 along the *x* and/or *y* axis. Throughout the simulations, parameters such as temperature, stress, and position of each atom were monitored as a function of time. The temperature, position of the atoms, and the pressure averaged across each face of the simulation volume were directly output from the simulations. Because for some cases the faces of the bar did not extend across the entire simulation volume, it was necessary to adjust the stress as follows. Large-scale Atomic/Molecular Massively Parallel Simulator (LAMMPS) co mputes the force on the entire simulation box face, the reported stress is this force divided by the simulation box face area. Since our sample bar is often smaller than the simulation box, the ratio of the area of the box face to the bar face is used to compute the stress on the bar face.

MD simulations were conducted using LAMMPS [13] implemented on the Lonestar5 cluster located in the Texas Advanced Computing Center at the University of Texas at Austin. The embedded atom method potential for Ag from the NIST Interatomic Potentials Repository Project was used [14, 15]. This potential has been further vetted for high strain-rate simulations by correctly computing c_{11} and c_{44} for uniaxial tensile and shear strain at strain rates of 1×10^9 , 2×10^9 , and 2×10^{10} s⁻¹ [9]. Bars with dimensions of 30 lattice constants (LC = 0.4089 nm) on a side that were initially free of grain boundaries or stacking imperfections were used to limit the parameter space to a reasonable number of variables. This sample geometry was selected to minimize surface effects that can otherwise dominate results when slender, nanowire, or spherical nanoparticle geometries are simulated. The sample cube was placed symmetrically in a $30 \times 30 \times 50$ LC simulation box with periodic boundary conditions in all dimensions. This resulted in a vacuum interface on the surfaces perpendicular to the z axis and continuous silver atoms at the periodic x and y simulation box faces.

The MD simulations were initialized by first allowing the bar to thermalize at 300 K for 40 ps with a time step of 0.001 ps (1 fs) using Nose–Hoover style, non-Hamiltonian equations of motion and the isothermal-isobaric integrator (called NPT)[16]. The bar was checked for energy equilibration for 10 ps (via the microcanonical, energy conserving integrator called NVE) before strain was applied. The subsequent deformations were applied using the NVE integrator so that only the input stress–strain energy could affect the potential energy (PE), kinetic energy (KE), and temperature of the sample. The simulations were found to be converged for a 1 fs timestep. Thermodynamic and stress variables were output at strain intervals of 0.005, and the positions of all atoms were output at intervals of strain of 0.01 to an upper limit of $\varepsilon=0.30$. LAMMPS commands were used to deform the sample along the desired dimensions at a constant engineering strain rate while simultaneously adjusting the simulation box to contain all the atoms. Thus, during the simulation, the atoms at the vacuum interface were never allowed to touch the edge of the simulation box, and therefore they did not interact across the periodic boundary.

The locations of the atomic positions were studied off-line using OVITO visualization software [17]. Qualitative assessments of the changes to the crystals were made using three dimensional visualizations of the atomic positions within the bar. In some cases, finite thickness sections through the bar that were several lattice parameters thick were visualized to further refine the observations.

The polyhedral template matching (PTM) algorithm within OVITO was used to identify the local atomic configurations for all atoms in the simulations [18], and thus to identify the mechanism(s) that resulted in the onset of permanent deformation. For example, plastic deformation at moderately high strain rates in fcc crystals results from the initiation and glide of Shockley partial dislocations [19]. The passage of a Shockley partial dislocation leaves a stacking fault with local hcp stacking. Thus, the presence of local regions of hcp stacking following deformation are a hallmark of plastic deformation caused by partial dislocation motion. At high strain rates, the periodic structure of the lattice may be lost when a disordering (amorphization) transformation occurs in the solid state. Continued application of stresses that are of a sufficiently large magnitude to the disordered lattice results in viscous flow. The disordering transformation and plastic flow by viscous deformation can be detected by OVITO, since these atoms are in a configuration that does not exhibit regular periodicity. Under some conditions, a phase transformation from fcc to bcc has also been observed as the fcc lattice is deformed [20, 21]. This transformation is second order because the bcc phase is formed continuously when the fcc lattice is severely distorted by large elastic strains. In contrast to dislocation initiation and propagation or disordering transformations/viscous flow, the bcc transformation does not dissipate significant strain energy.

The PTM values for individual atoms were color-coded with green representing local regions with fcc coordination, red representing regions with local hcp coordination, and blue representing local bcc coordination. When the atomic coordination could not be identified (e.g. at surfaces or where the atoms were disordered), atoms were defined as other and colored gray. The transition from fcc to hcp or fcc to disordered that is identified using PTM is dependent on the value of the user-defined root-mean-square displacement (RMSD) cutoff parameter. If the RMSD parameter is set too low, atoms which are clearly ordered based on visualizations of the atomic structure are incorrectly labeled as disordered. If the RMSD parameter is set too high, then the opposite is true; atoms that clearly have disordered are incorrectly labeled as ordered. Thus, in practice, the RMSD cut-off parameter must be varied and compared to the visualizations to determine a reasonable value where few if any atoms are mislabeled. For the simulations conducted for this study, a RMSD cut-off parameter value of 0.15 was found to give good agreement between qualitative observations and the results from PTM.

A quantitative criterion to assess changes in PTM classification of local atomic structure was employed; the onset of *any* type of structure change was defined for this study by a 10% *decrease* in the number of fcc atoms. A 10% *increase* of other atoms, hcp atoms, or bcc atoms was used to identify the *onset* of disordering, dislocation initiation, or bcc phase transition, respectively. The simulation bar was deemed to have fully disordered if there was at least an initial 10% increase in other atoms that was followed at increasing strains by an increase of other atoms to at least 50% of the total atoms present in the sample. To supplement PTM analysis, dislocation analysis (DXA) [22] was used in OVITO to visualize, identify by type, and count dislocation numbers based on their Burgers vector.

Total KE, KE/atom (which is proportional to average temperature), total PE of the entire system of atoms, and PE/atom, are all standard variables within LAMMPS, and they were output for graphing and visualization in OVITO. Because uniform strains were applied for the simulations and the number of surface atoms was small, it is reasonable to assume that average values of the PE/atom, KE/atom, and temperature are representative of bulk values after subtracting the contribution of the surface atoms. In all our computations and graphs involving PE/atom, the contributions from all atoms present within the sample were averaged after excluding the contributions from surface atoms.

3. Results

To study disorder onset as a function of biaxial strain rate, we first examine in detail two representative strain rates and strain states where plastic deformation results from either dislocation motion, $\dot{\varepsilon} = 1 \times 10^9 \, \mathrm{s}^{-1}$, or from disorder followed by viscous flow, $\dot{\varepsilon} = 1 \times 10^{11} \, \mathrm{s}^{-1}$.

3.1. Strain in the (11 $\overline{2}$) plane at strain angles of -45° and 135°; strain rate $= 1 \times 10^9 \text{ s}^{-1}$

Recalling that the simulations are conducted by applying strains on two orthogonal faces of the bar at a fixed strain rate and computing the resulting stresses, we begin by considering a representative stress versus strain plot. Figure 2(a) shows the tensile (right side/positive) and compressive (left side/negative) biaxial stress versus strain response for a bar oriented such that the strain in the x direction is applied in the $(11\overline{2})$ [111] while imposing a strain of equal magnitude in the -y direction in the $(11\overline{2})$ [110] (strain angles of -45 and 135°). The figure shows that the stress versus strain response at small strains in both the x and y directions is linear when a tensile strain is applied in the x direction and a compressive strain is applied in the y direction. As the strains approach 0.04, there is non-linearity as expected for such large strains/stresses. Beyond this strain, a yield point occurs in tension for strains larger than 0.05,

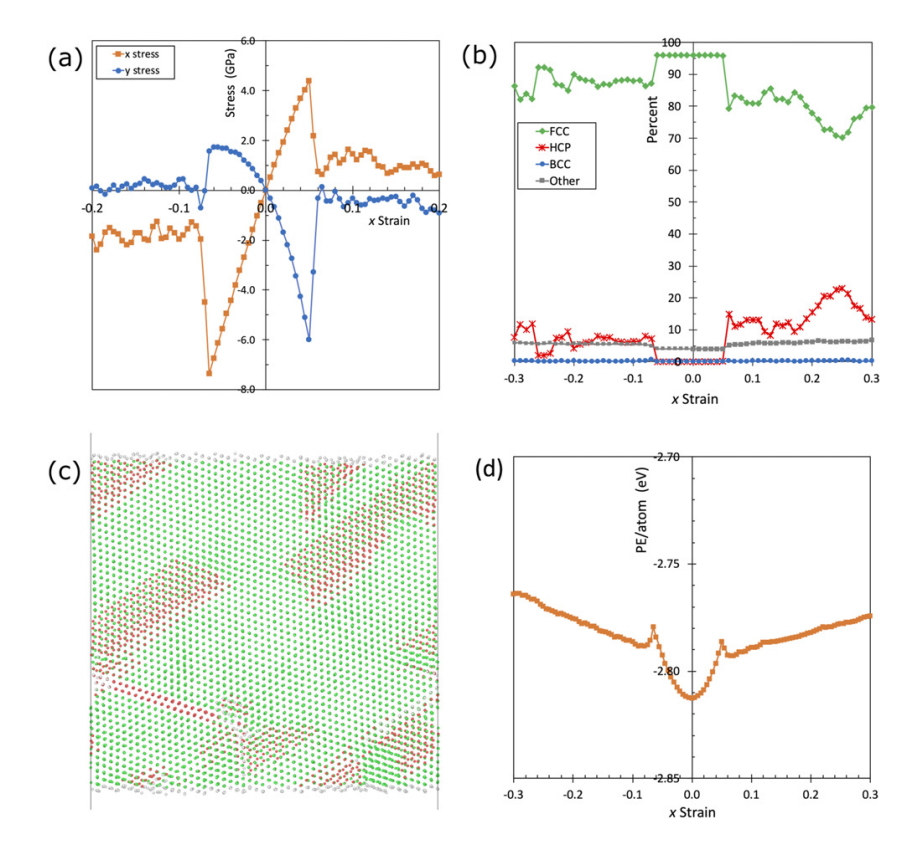


Figure 2. Simulation results for strain angles of -45° and 135° at a rate of 1×10^{9} s⁻¹ in the $(11\overline{2})$ plane: (a) x and y stress components vs applied x strain; (b) percent of atoms identified by PTM vs x strain; (c) 1.5 nm thick cross section of the bar with $\{110\}$ faces at an x strain of +0.06 near the yield point, which shows dislocations in three of the four $\{111\}$ planes, one of which is seen on-edge in this $\langle 110 \rangle$ view; and (d) PE/atom vs x strain. In (c), fcc atoms are green, hcp atoms are red, and other atoms are gray.

followed by a discontinuous decrease in the magnitude of the stress when the ultimate tensile stress is reached. At still larger strains, discontinuous yielding is apparent. The tensile and compressive responses are qualitatively similar, except that the yield point and ultimate tensile stress occur at larger strains in compression.

Figure 2(b) shows that the lattice initially consists of atoms mostly with an fcc coordination with a small fraction of other atoms, which are located at the surface of the bar. The yield point is accompanied by a discontinuous decrease in fcc atoms and a corresponding increase in hcp atoms associated with the nucleation and motion of dislocations. The number of other atoms remains approximately constant. Figure 2(c) shows that at a strain of 0.06 where significant plastic strain is apparent in figure 2(a), stacking faults are present on three of the four {111} planes. DXA indicates that these defects result primarily from the motion of Shockley dislocations (86% of the reported dislocation length), some of which intersect at stair-rod dislocations (9% of the reported dislocation length). When viewed parallel to a {111} plane,

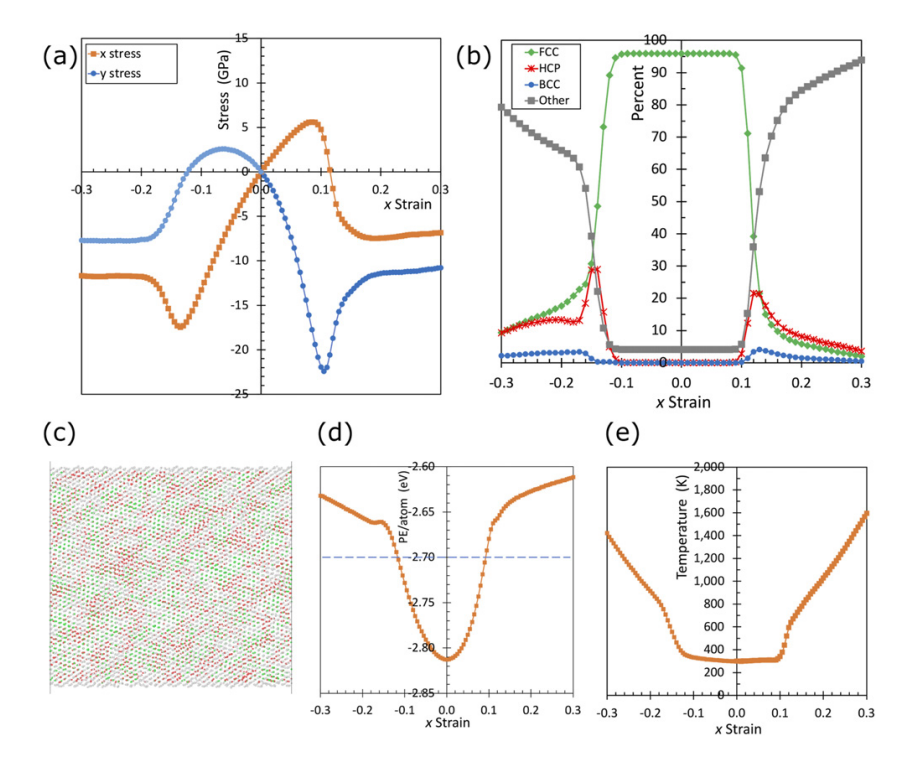


Figure 3. Simulation results for strain angles of -45° and 135° at a rate of $1 \times 10^{11} \, \mathrm{s}^{-1}$ in the $(11\overline{2})$ plane: (a) x and y stress components vs applied x strain; (b) atomic configurations of atoms vs x strain; (c) 1.5 nm thick cross section of the bar with $\{110\}$ faces, just after disordering at an x (horizontal) strain of +0.13, at which point there are 56% other atoms, 22% fcc atoms, and 22% hcp atoms; (d) PE/atom vs x strain; and (e) temperature vs x strain. In (c), fcc atoms are green, hcp atoms are red, other atoms are gray, and bcc atoms are blue.

this pair of stacking faults are 2 to 4 atom planes thick. A plot of PE/atom versus strain is shown in figure 2(d). This plot has the expected nearly parabolic response at small strains when energy input into the system is stored as elastic strain energy. As the stress peaks and begins to decrease at an x strain of +0.05 and -0.07, there is a sharp deviation from a parabolic response when energy is channeled into initiating and moving dislocations. Significantly, the PE/atom remains well below the expected threshold for disordering of -2.7 eV.

3.2. Strain in the $(11\overline{2})$ plane at strain angles of -45° and 135° ; strain rate $= 1 \times 10^{11} \text{ s}^{-1}$

Figure 3 shows the responses of a crystal with the same orientation and strain state as that shown in figure 2, but at a higher strain rate of $1\times 10^{11}~\rm s^{-1}$. The stress versus strain response at this higher strain rate is qualitatively different than at the slower rate shown in figure 2. The tensile stress–strain response exhibits greater non-linearity at larger strains, the drop in stress beyond the ultimate tensile stress is less sharp, and discontinuous yielding is no longer observed. The ultimate tensile strength is also larger at the faster strain rate. The response at

this strain rate is similar when a compressive stress is applied along the x direction, except that ultimate tensile stress is much larger (17 GPa). Figure 3(b) shows that by a strain of +0.11 and -0.13, the number of fcc atoms drops sharply and there is small increase in the number of bcc atoms and hcp atoms and a much larger and immediate increase in the number of other atoms. This plot shows that disordering and deformation by viscous flow are observed when either compressive or tensile strains are applied at this strain rate.

Figure 3(c) shows a snapshot of atomic positions at a strain + 0.13 where it is apparent that atoms with an hcp configuration (shown in red) appear in patches that are extremely short stacking faults caused by the motion of partial dislocations. The disordered regions are homogenously distributed and appear to initiate near the edges of the dislocations. The percentage of atoms in an hcp configuration begins to decrease as the percentage of disordered, other atoms continues to increase with strain in homogeneously distributed patches to a percentage above 50%. A plot of PE/atom versus strain is shown in figure 3(d). This plot again shows the nearly parabolic response when the stress–strain response is elastic. As the stress peaks and begins to decrease at an x strain of +0.11 and -0.13, there is a sharp deviation from a parabolic response when the PE/atom exceeds approximately -2.7 eV atom⁻¹ and energy is channeled into initiating and moving dislocations, disordering the lattice, and viscous deformation. There is also a corresponding rapid temperature increase during this strain regime where there is extensive plastic deformation (figure 3(e)). Note that although the temperature exceeds the equilibrium melting temperature for Ag of 1235 K when the strains exceed ± 0.20 , the bar is more that 80% disordered in the solid state before the melting temperature is reached.

3.3. Influence of strain rate and strain state on transformation from fcc configuration

Figures 2 and 3 show that for strain angles of -45° and $+135^{\circ}$, deformation results from dislocation motion at relatively low strain rates and transitions to disordering/viscous flow at higher strain rates. We now introduce a second variable, strain state, and characterize the mechanisms that result in permanent deformation when a range of biaxial strain states are applied.

Figure 4(a) presents the strain vector components required to produce a 10% decrease in the number of atoms with an fcc configuration. Data is presented for a range of strain rates and strain states/strain angles for loading in the $(11\overline{2})$. This plot allows direct visualization of the influence of strain state on the strains required to transform atoms to another configuration. For example, 0° on this plot corresponds to an applied tensile strain in the positive x direction (with y strain fixed at zero), 45° corresponds to equibiaxial (x and y) tension, and so on.

Figure 4(a) shows that for biaxial loading, as the strain rate is increased, there is a nearly uniform expansion of the transformation surface that indicates that the transformation is delayed to larger strains as the strain rate is increased, independent of strain angle. For example, the strain when 10% of the fcc atoms are transformed is about 50% larger for a $\dot{\varepsilon}=1\times10^{11}~{\rm s}^{-1}$ compared to $\dot{\varepsilon}=1\times10^9~{\rm s}^{-1}$. The dashed lines show the strain vector components required for a 10% increase in the number of atoms identified as other for strain rates of $1\times10^{11}~{\rm s}^{-1}$ and $4\times10^{11}~{\rm s}^{-1}$ —the two strain rates where significant disordering occurs for loading in this crystallographic orientation. The surfaces that define the transition to atoms with an other configuration are nearly concentric with those for the transformation from an fcc configuration. This indicates that the transformation from fcc primarily results in disordering rather than dislocation motion at these strain rates. The transformation surfaces for all strain rates are relatively isotropic which suggests that strain state does not strongly affect the onset of transformation for loading along these specific crystallographic directions.

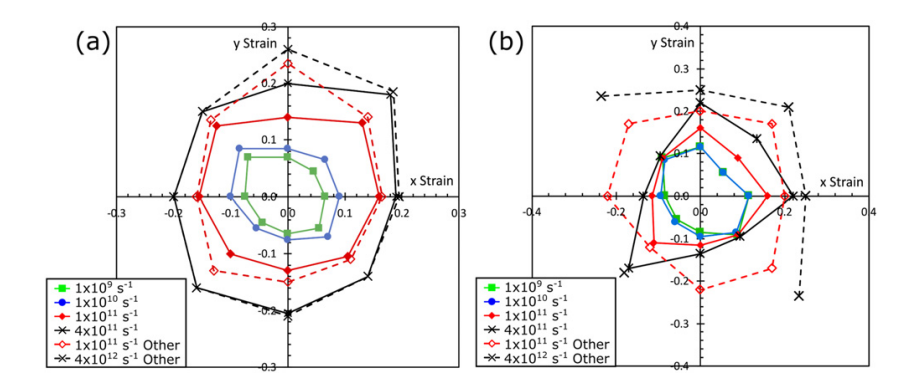


Figure 4. Strain vector components required to induce a 10% decrease in number of fcc atoms (solid lines) and strain vector components required to induce a 10% increase in other atoms (dashed lines): (a) loading in the $(11\overline{2})$ plane where the x direction is [111] and the y direction is [1\overline{1}0]; (b) loading in the (001) plane where the x direction is [100] and y direction is [010].

Figure 4(b) shows a plot where the strain is applied in the (001) plane where the x direction is loaded along the [100] and the y direction is loaded along the [010]. As was observed in figure 4(a), there is a general trend where the transformation is delayed to larger strains as the strain rate is increased. However, compared to figure 4(a), this transformation surface is far less isotropic. The strains required to transform from an fcc configuration for strain angles 0°, 90° , and -135° are higher than for the other five strain angles. On the other hand, the transformation to an other configuration in the (001) plane occurs at more uniform strains than the corresponding strains where fcc atoms begin to transform. This delay in disordering at the five strain angles that transform from fcc at lower strain suggests that the initial deformation for this crystallographic orientation occurs by a combination of dislocation motion, bec transformation, and disordering; and it is consistent with a more sluggish disordering transformation that may also be inhomogeneous. The cause for this delay in disordering will be explored further in a later subsection. Overall, the plots in figure 4 show that the strain required for transformation from an fcc configuration generally increases with strain rate. However, this strain is also affected by the strain state, the crystallographic planes that the strains are applied in, and the strain state/direction.

3.4. PE/atom below and above the threshold for disordering

Because we are particularly focused on disordering behavior, we now turn our attention to correlations between strain state, strain rate, the PE/atom, and the observed disordering behavior.

3.4.1. PE/atom for biaxial strain in the (11 $\overline{2}$) plane. Figure 5 shows a plot of PE/atom versus strain for a range of strain angles and strain rates (figures 5(a)–(d)) and the corresponding percentages of each atom configuration for the specific strain rate of $\dot{\varepsilon}=1\times 10^{11}~\text{s}^{-1}$ (figures 5(e)–(h)). Figure 5(a) shows PE/atom versus strain for strain angles of -45° (right/positive side of plot) and $+135^{\circ}$ (left/negative side of plot). The initial PE/atom when there is no applied strain is approximately -2.81~eV. Applying either uniaxial tensile or compressive loading results in a nearly parabolic increase in PE/atom at small strains, consistent

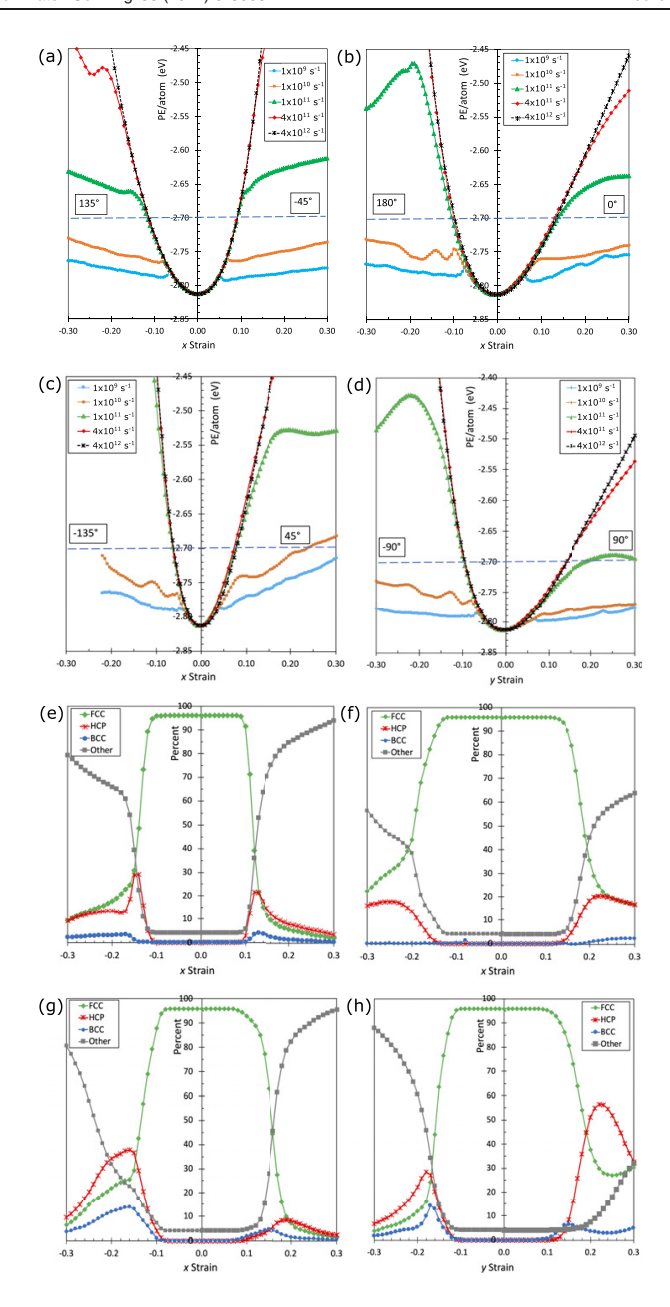


Figure 5. PE/atom vs strain for all eight strain orientations and strain rates for strain in the $(11\overline{2})$ plane, (a)–(d), and corresponding percentages of atoms at $\dot{\varepsilon} = 1 \times 10^{11} \text{ s}^{-1}$ with configurations of fcc, hcp, bcc or other versus strain, (e)–(h). In (d) and (h), y strain is plotted since the x strain is constrained to be zero.

with the expected linear elastic loading at small strains. The PE/atom response is slightly asymmetric between tensile and compressive responses because engineering strain is plotted rather than true strain and because the atomic force potentials are also asymmetric, especially at larger strains.

As the magnitude of the strain is increased further, there is a deviation from parabolic response that is particularly sharp at lower strain rates. For example, for a $\dot{\varepsilon}=1\times10^9~{\rm s}^{-1}$, there is a sharp deviation from parabolic behavior at an x strain of ± 0.05 . Comparing this x strain magnitude shown in figure 5(a) for $\dot{\varepsilon}=1\times10^9~{\rm s}^{-1}$ to the plots shown in figures 4(a) and 2(b), it apparent that this is also the strain where a significant fraction of fcc atoms has begun to transform. When the strain rate is increased by an order of magnitude to $\dot{\varepsilon}=1\times10^{10}~{\rm s}^{-1}$, the sharp deviation from parabolic response occurs at a slightly larger x strain of approximately +0.07 and -0.08. This again corresponds to the x strain where a significant fraction of fcc atoms has begun to transform according to figure 4(a). As the strain rate is increased still further to $\dot{\varepsilon}=1\times10^{11}~{\rm s}^{-1}$, the deviation from nearly parabolic response shifts to still larger x strain, but also becomes less sharp. These trends continue at the higher strain rate of $\dot{\varepsilon}=4\times10^{11}~{\rm s}^{-1}$ with even more gradual deviations from parabolic responses that occur at increasingly larger x strain.

For a strain rate of $\dot{\varepsilon}=1\times10^9~{\rm s^{-1}}$, the sharp break from nearly parabolic response occurs at a PE/atom of $-2.79~{\rm eV}$ atom $^{-1}$ for this strain state and loading plane. Examination of the atomic configurations at a PE/atom below and above these levels reveals that the sharp deviation occurs when plastic deformation due to dislocation nucleation occurs near the specimen surfaces. Increasing the strain rate to $\dot{\varepsilon}=1\times10^{10}~{\rm s^{-1}}$ increases the PE/atom where the sharp break occurs to -2.78 (tension) to $-2.76~{\rm eV}$ atom $^{-1}$ (compression), but the trends observed at the lower strain rate are otherwise similar. This shows that the onset of plastic deformation due to dislocation motion is delayed to higher PE/atom, strain, and stress as the strain rate is increased.

When the strain rate is increased still further to $\dot{\varepsilon}=1\times10^{11}~{\rm s}^{-1}$, there is an additional increase in the PE/atom at which it deviates from a nearly parabolic response. For this strain rate, the PE/atom slightly exceeds $-2.70~{\rm eV}$. Figure 5(e) shows that at $\dot{\varepsilon}=1\times10^{11}~{\rm s}^{-1}$, the transformation from an fcc configuration occurs simultaneously with a large increase in the number of other atoms and a smaller increase in the atoms with an hcp configuration and still smaller increase in the number of atoms with a bcc configuration. For a higher strain rate of $\dot{\varepsilon}=4\times10^{11}~{\rm s}^{-1}$, figure 5(a) shows that the PE/atom significantly exceeds $-2.70~{\rm eV}$, and the deformation now results almost completely from disordering accompanied by viscous flow.

Figure 5(b) shows a plot of PE/atom versus strain in the x direction for strain angles of 0° (tensile/right side of plot) and $+180^{\circ}$ (compressive/left side of plot). The compression response for these strain angles is stiffer than the tensile response because the elastic and plastic response for this orientation of the single crystal is more anisotropic for these strain directions. These plots for plane strain tension and compression are otherwise similar to the plots shown in figure 5(a); they show nearly parabolic response at low strain magnitudes, sharp deviations from parabolic response at low strain rates when plastic deformation results from dislocation motion, and a delay in plastic deformation with a transition to disordering at higher strain rates. For a $\dot{\varepsilon}=1\times10^{11}~{\rm s}^{-1}$, the PE/atom significantly exceeds $-2.70~{\rm eV}$, and figure 5(f) shows that more than 50% of the atoms disorder before the strain reaches 0.3.

The PE/atom versus strain response for strain angles of -135° and $+45^{\circ}$ is still stiffer than for strain angles of 180 and 0° as seen by the steeper PE/atom curves for tension and compression, but they are otherwise similar. Notably, for both strain directions, disordering is only observed when the PE/atom exceeds -2.70 eV atom⁻¹ (figures 5(c) and (g)) at strain rates of $\dot{\varepsilon}=1\times10^{11}~\rm s^{-1}$ and higher.

Figure 5(d) shows the PE/atom response for strain angles of -90° and $+90^{\circ}$, i.e. plane strain tension and compression along the y axis. Since the major strains are applied along the y axis for this case, the abscissa is the strain applied along the y direction. For a strain angle of -90° , the behavior is much the same as the previous cases. The PE/atom versus strain response for a 90° strain angle is notable because it exhibits the lowest stiffness of the strain angles that were examined, and the resistance to plastic deformation was also low. Thus, compared to other strain angles, dislocation motion is initiated relatively easily. Unlike other strain angles, for a strain angle of $+90^{\circ}$ and a strain rate of $\dot{\varepsilon} = 1 \times 10^{11} \text{ s}^{-1}$, the PE/atom exceeds -2.70 eVby only 0.05 eV. Figure 5(h) shows that deformation when the PE/atom exceeds -2.70 eV initially results primarily from dislocation motion accompanied by a large fraction of atoms transforming to an hcp configuration. As the PE/atom increases further, the number of dislocations (% hcp) begins to decrease as the fraction of atoms that disorder increases rapidly. Although the fraction of disordered atoms is still increasing, it only reaches about 32% at a y strain of 0.3 and peaks at 42% below a strain of 0.5. So, the crystal does not fully disorder at this strain rate and strain direction. This result is anomalous in that the PE/atom slightly exceeds -2.70 eV, but disordering is incomplete. Further examination of the atomic images for this case will show that the transformation is inhomogeneous, and that disordering occurs in local regions that satisfy the minimum PE/atom criterion. Details for this case will be presented later in the discussion section. In summary, the results for strain in the $(11\overline{2})$, show that a critical minimum PE/atom of -2.70 eV can be used to predict the onset of the disordering transformation under biaxial loading.

Simulations at a strain rate of $\dot{\varepsilon}=4\times10^{12}~{\rm s}^{-1}$ were conducted to show the shape of the PE/atom vs strain curve when the atoms did not form dislocations or disorder. At this high strain rate, there was insufficient time between the sampled atom images for either dislocation initiation or disordering to occur. No change in the number of fcc atoms is seen at this high strain rate, and the PE/atom curve does not show a break. The $\dot{\varepsilon}=4\times10^{12}~{\rm s}^{-1}$ curve is useful for visualizing deviations in the other PE/atom curves when dislocation nucleation or disordering occurs for the lower strain rates.

3.4.2. PE/atom for biaxial strain in the (001) plane. To further test if the hypothesis that PE/atom can be used to predict the onset of disordering during biaxial loading, additional strain states were considered for biaxial loading within the (001) plane in the x=[100] and y=[010] directions. These cases produced results that are substantially similar to the cases for strain in the $(11\overline{2})$ plane. When PE/atom exceeds -2.70 eV, disordering ensues, and there is a break in the PE/atom curve at that point. Furthermore, the stress does not begin to decrease until the PE/atom reaches the break point. The differences from the cases for strain in the $(11\overline{2})$ will be noted and discussed. These differences are: (1) there is no disordering for strain angles of $-45^{\circ}/135^{\circ}$ at $\dot{\varepsilon}=1\times10^{11}~{\rm s}^{-1}$, (2) the changes in atomic % show more variation with strain angle, and (3) for five strain angles, a significant fraction of the atoms transition to a bcc configuration.

Figure 6 presents PE/atom versus (001) plane strain for the same eight strain angles shown in figures 5(a)–(c) and the corresponding percentages of atom configurations (d)–(f). Note that for strain in the (001), some of the strain angles are identical by symmetry and have identical plots in figure 6. For the lower strain rates of $\dot{\varepsilon}=1\times10^9~{\rm s^{-1}}$ and $1\times10^{10}~{\rm s^{-1}}$ and for all strain angles, the PE/atom versus strain response is similar to the response observed for loading in the (11 $\overline{2}$) plane. The sharp break in the PE/atom curve is accompanied by dislocation nucleation and motion, and the PE/atom remains well below the expected threshold for disordering of $-2.70~{\rm eV}$. The variation with strain angle at these lower strain rates is generally small except for a somewhat lower onset for plastic deformation for strain at 45° (equibiaxial tensile) as

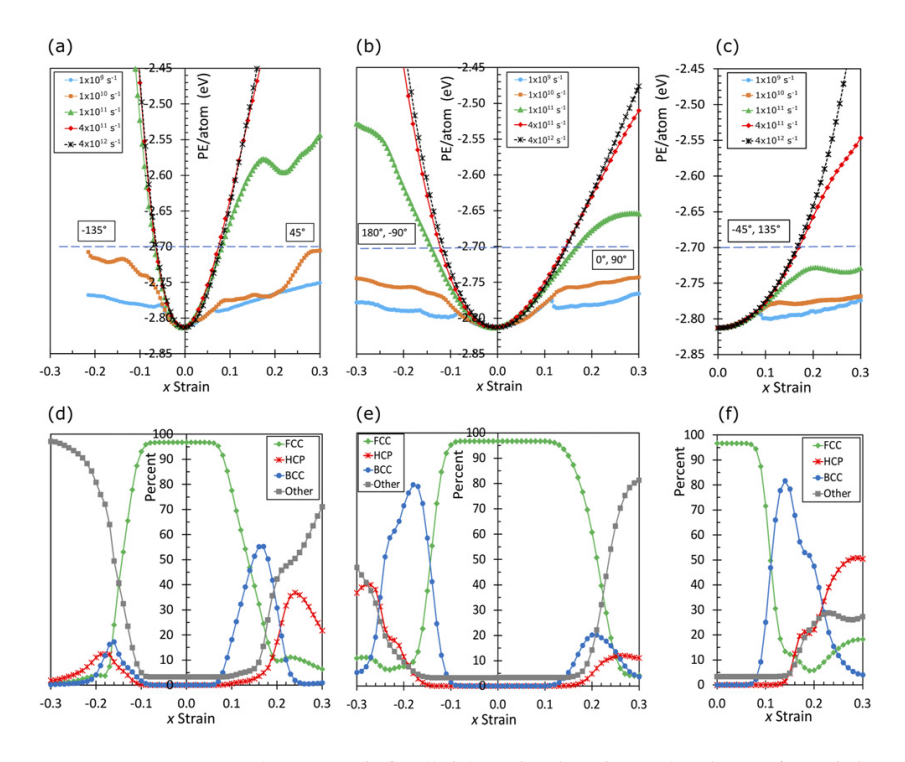


Figure 6. PE/atom vs strain for all eight strain orientations and strain rates for strain in the (001) plane, (a)–(c) and corresponding percentages of atoms at $\dot{\varepsilon}=1\times10^{11}~\rm s^{-1}$ with configurations of fcc, hcp, bcc or other versus strain, (d)–(f).

seen in figure 4(b) (10% decrease in fcc atoms) and figure 6(a) (break in the PE/atom vs strain curves)

At a strain rate of 1×10^{11} s⁻¹, the PE/atom rises above -2.70 eV for six strain angles as shown in figures 6(a) and (b), and disorder ensues as seen in figures 6(d) and (e) by the increase of other atoms. For the remaining (symmetrically identical) two strain angles of $-45^{\circ}/135^{\circ}$, PE/atom does not surpass -2.70 eV until the strain rate increases to 4×10^{11} s⁻¹. For this higher strain rate, disorder does occur as predicted by the PE/atom increase above -2.70 eV. For the two higher strain rates of 1×10^{11} s⁻¹ and 4×10^{11} s⁻¹, the three angles that do not show bcc phase formation, 0° , 90° , and -135° , have a higher onset strain for a 10% decrease in fcc atoms. They also behave similarly to the $(11\overline{2})$ cases in that the gap between a 10% decrease in fcc atoms and the 10% increase in other atoms is small (figure 4(b)). The other five strain angles are soft for plastic deformation but slow to disorder. The transition to disorder is from atoms primarily with a bcc configuration, and the transition is delayed to higher strain values as seen in the larger gaps between the 10% fcc atom decrease and the 10% other atom increase curves in figure 4(b).

As before, figure 6 has PE/atom curves for a strain rate of $\dot{\varepsilon}=4\times10^{12}~{\rm s}^{-1}$. Again, no change in the number of fcc atoms is seen, and the PE/atom curve does not show a break. This curve is used to visualize deviations of the other curves obtained at lower strain rates.

The results from figures 5 and 6 show that for all combinations of applied biaxial strains in the $(11\overline{2})$ and (001) planes, deformation results from dislocation motion at strain rates $\dot{\varepsilon}=1\times10^{10}~\rm s^{-1}$ and below and that the resistance to dislocation nucleation and propagation increases with strain rate for all strain angles. For each of the cases that were studied, the onset of disordering was observed only when the PE/atom exceeded $-2.70~\rm eV$. This result is consistent with the hypothesis that a critical minimum PE/atom of $-2.70~\rm eV$ is a material property that can be used to predict the minimum strain rate for disordering for any strain state.

4. Discussion

We now consider whether the hypothesized disorder criteria have been met for all the configurations of anisotropic strain that were simulated. An apparent discrepancy will be discussed and resolved as a case of inhomogeneous behavior.

4.1. Agreement with the hypothesized criteria

The hypothesized conditions for disorder during biaxial loading are as follows: (1) a fixed minimum PE/atom for each material is required for the disorder transition to occur; (2) a minimum strain rate is required for the disorder transition to occur, and it may vary with the orientation of the crystal lattice and strain state; and (3) for applied strain rates greater than the minimum required for disorder, the disorder transition is delayed and occurs at a higher PE/atom than the critical threshold.

The critical PE/atom for Ag was derived from melting simulations to be -2.70 eV, and this was confirmed for uniaxial deformation simulations [9]. The same critical PE/atom is now demonstrated for biaxial strain applied to Ag as shown in figures 5 and 6 with one possible exception noted for strain at 90° in $(11\overline{2})$ that will be explained in the next section. Fluctuations in PE/atom observed in the simulations are in the last digit of the reported critical value of -2.70 eV (2nd digit after the decimal). In the examples of figures 2 and 3, the standard deviation for figure 2 increased from 0.023 eV when no strain was applied to 0.026 eV at a strain just before dislocations nucleated. At the higher strain rate of figure 3, the standard deviation increased to 0.036 eV just before the onset of disordering. This establishes the confidence level of the critical value of PE/atom for disordering.

Furthermore, it was shown that the strain rate for the onset of disorder is not a material property and was found to vary for biaxial loading between $\dot{\varepsilon}=1\times10^{11}~{\rm s}^{-1}$ and $\dot{\varepsilon}=4\times10^{11}~{\rm s}^{-1}$. Figures 5 and 6 also show that for strain rates higher than the minimum required, the break in the PE/atom curve and the onset of disordering is shifted to a larger PE/atom value. This suggests that over short times (ps) additional strain energy may be stored in the lattice PE (indicated by the undeviated PE/atom curve) until the onset of disorder allows the release of this energy and an abrupt temperature rise. Similar behavior was observed for uniaxial loading.

4.2. Inhomogeneous disordering at 90° in the $(11\overline{2})$ plane

For the one case of a strain angle of 90° in the $(11\overline{2})$ where only partial disorder occurred at a critical PE/atom of -2.70 eV, examination of the atom images using OVITO empirically shows nonuniform atomic configurations. In figure 7(a), there is a somewhat nonuniform distribution of dislocations and hcp atoms at a strain of 0.20, and in figure 7(b) there is a notably larger concentration of other atoms near the center of the bar at a strain of 0.32. This nonuniformity is easily quantified using the atom groups illustrated in figure 7(c) for the core atoms and near-surface atoms. Each group contained 8000 to 10000 atoms and extended through the whole

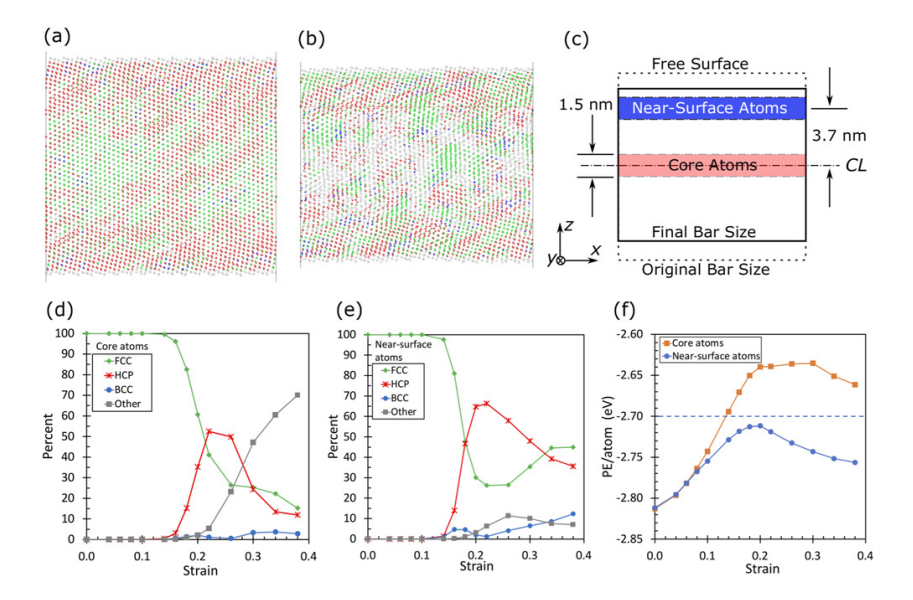


Figure 7. Behavior of core atoms and near-surface atoms for a strain rate of 1×10^{11} s⁻¹ at 90° in the (11 $\overline{2}$) plane. 1.0 nm thick cross sections of the bar with {110} faces, at strain 0.20 and 0.32 are shown in (a) and (b), respectively. (c) {110} diagram of the location of the two sampled regions of atoms: core atoms and near-surface atoms. In (d) and (e), the atom configuration percentages vs y strain are plotted for core and near-surface atoms respectively. In (f) the PE/atom vs y strain is plotted for both the core and near-surface atoms. In (a) and (b), fcc atoms are green, hcp atoms are red, other atoms are gray, and bcc atoms are blue.

thickness of the bar in the y direction. Atoms within two layers of the free surface were excluded from the near-surface group because they were always classified as other.

When the local atomic configuration percentages were calculated for the two groups of atoms, there were marked differences as shown in figures 7(d) and (e). For the core, the percentage of other atoms rose above 65%, and so this region is classified as disordered. The opposite is true for the near-surface atoms, which retain a high defect density and where the other atoms never exceed 15%. Finally, as predicted by the hypothesized criteria for disordering, the simulations reveal significant differences in the PE/atom vs strain behavior for the two groups, as shown in figure 7(f). The core atoms clearly exceed -2.70 eV, whereas the near-surface atoms do not reach the critical PE/atom value. The PE/atom for these two regions is clearly predictive of their atomic disordering behavior in accordance with the critical PE/atom hypothesis.

Visualizations of the atoms shown in the section images of figures 7(a) and (b) at strains of 0.20 and 0.32 respectively, show that the atoms experience non-uniform strains and strain states evidenced by distortions of the lattice and bending of the lattice planes near the free surface. This results from the significant elastic and plastic anisotropy for this crystallographic orientation. These non-uniform strains result in a very different configuration of atoms near the free surface where figure 7(e) shows that the atom distribution is dominated by hcp atoms and the percentage of other atoms never exceeds 15%.

It was previously shown that the PE/atom criterion can be used to predict the minimum strain rate required to initiate disordering for a homogenous uniaxial strain state [9]. In the first part of the present paper, we have shown that the same criterion can be used to predict disordering for a homogenous biaxial strain state. When inhomogeneous strain states arise, figure 7 demonstrates that the PE/atom criterion can also be used as a predictor for disordering when the minimum strain rate requirement is met. This result opens the possibility of applying this criterion to predicting disordering when highly non-uniform strain states arise, such as when sub-micron particles strike surfaces. In a future paper, we will explore the feasibility of using this approach to predict disordering during the micro-cold spray film formation process where nano-scale particles impact onto a substrate at velocities more than $100 \, \mathrm{m \, s^{-1}}$, and strain rates more than $\dot{\varepsilon} = 1 \times 10^{11} \, \mathrm{s^{-1}}$ are encountered.

5. Conclusions

We have studied whether critical PE/atom can be used to predict the onset of disordering at high strain rates under biaxial loading. The starting point for this hypothesis is a recently proposed theory to predict solid-state disordering based on a critical PE/atom that was previously applied to uniaxial strain states. The critical PE/atom for uniaxial loading was found to be -2.70 eV for fcc silver based both on its melting behavior and on its disordering when high uniaxial strain was applied [9]. The critical PE/atom criterion is notable because, in contrast to previous theories, it incorporates the effect of strain rate and is agnostic to whether the applied strain is uniaxial or biaxial.

To investigate the validity of this disorder criterion for biaxial strain, MD simulations of fcc Ag were conducted over a wide range of biaxial strain rates, strain configurations, and crystal orientations with respect to the applied stress state. Biaxial strains were applied in two different planes, $(11\overline{2})$ and (001) in eight directions in each plane. The strains were resolved into two orthogonal components which could be positive, negative or zero, and the components were in the orthogonal coordinate directions of the sample bar. The resulting strains were characterized by their strain angle, which is the angle of the vector sum of the orthogonal +x and +y applied strain components.

Results from simulations showed that at relatively low strain rates, the response was the expected response; elastic deformation was observed at small strains, followed by plastic deformation when the nucleation and propagation of dislocations occurred above a critical strain. The yield stress was observed to increase with strain rate. As the strain rate was increased further, disorder initiated. The critical strain rate was found to vary in the range of $\dot{\varepsilon}=1\times10^{11}~\rm s^{-1}$ to $\dot{\varepsilon}=4\times10^{11}~\rm s^{-1}$, depending on the orientation of the crystal and the strain angle. This confirmed that the critical strain rate to initiate disorder is a not a material property. However, a consistent minimum PE/atom was observed before disordering occurred for a broad range of strain states and for both crystallographic orientations that were studied. This indicates that the critical PE/atom is a material property that can be used to predict the onset of disordering under biaxial loading.

For some strain states in the highly symmetric (001) plane, the atomic configuration was observed to change to bcc via a continuous decrease in the lattice parameter in one direction. The bcc phase that was observed in this case still obeyed the critical PE/atom necessary for disordering, albeit at a higher absolute strain value. For another case, a strain angle of 90° applied in the (11 $\overline{2}$), the critical PE/atom criterion was initially not definitive because it appeared that the critical PE/atom was exceeded, but only partial disordering was observed. This case was resolved when it was shown that the sample exhibited a non-uniform strain state that required that it be considered as two separate regions: the core atoms which did meet the

criterion and did disorder, and the near surface atoms which did neither. This case brings up the possibility that the PE/atom criterion for disordering may apply to situations of inhomogeneous strains or strain states. Such a scenario would occur for a nanoparticle impact onto a substrate at $100-1000 \, \mathrm{m \ s^{-1}}$ where the stress state, temperature, and strain rate vary with location within the nanoparticle and with time. There have been reported simulations that suggest that the PE/atom criterion can be utilized to predict local disordering within the nanoparticle and substrate if the PE/atom is tracked for individual atoms as a function of time [23, 24].

Acknowledgments

This work was supported by the National Science Foundation under Grant No. CMMI 2102818. The authors acknowledge the Texas Advanced Computing Center (TACC) at The University of Texas at Austin for providing LONESTAR5 (Cray Linux HPC cluster) resources that have contributed to the research reported in this paper. URL: http://tacc.utexas.edu.

Data availability statement

The data that support the findings of this study are available upon reasonable request from the authors.

ORCID iDs

Michael F Becker https://orcid.org/0000-0003-2992-9756 Desiderio Kovar https://orcid.org/0000-0002-1810-7653

References

- Ikeda H, Qi Y, Çagin T, Samwer K, Johnson W L and Goddard W A 1999 Strain rate induced amorphization in metallic nanowires *Phys. Rev. Lett.* 82 2900–3
- [2] Branício P S and Rino J-P 2000 Large deformation and amorphization of Ni nanowires under uniaxial strain: a molecular dynamics study *Phys. Rev.* B 62 16950–5
- [3] Koh S J A, Lee H P, Lu C and Cheng Q H 2005 Molecular dynamics simulation of a solid platinum nanowire under uniaxial tensile strain: temperature and strain-rate effects *Phys. Rev.* B 72 085414
- [4] Koh S J A and Lee H P 2006 Molecular dynamics simulation of size and strain rate dependent mechanical response of fcc metallic nanowires Nanotechnology 17 3451–67
- [5] Han S, Zhao L, Jiang Q and Lian J 2012 Deformation-induced localized solid-state amorphization in nanocrystalline nickel Sci. Rev. 2 493
- [6] Ogawa H 2005 Molecular dynamics simulation on the single particle impacts in the aerosol deposition process Mater. Trans. 46 1235–9
- [7] Ogawa H 2006 Atomistic simulation of the aerosol deposition method with zirconia nanoparticles Mater. Trans. 47 1945–8
- [8] Ghosh D, Subhash G, Zheng J Q and Halls V 2012 Influence of stress state and strain rate on structural amorphization in boron carbide J. Appl. Phys. 111 063523
- [9] Becker M F and Kovar D 2020 A quantitative criterion for predicting solid-state disordering during high strain rate deformation J. Phys.: Condens. Matter 33 065405
- [10] Voronel A, Rabinovich S, Kisliuk A, Steinberg V and Sverbilova T 1988 Universality of physical properties of disordered alloys *Phys. Rev. Lett.* 60 2402–5
- [11] Lam N Q and Okamoto P R 1994 A unified approach to solid-state amorphization and melting MRS Bull. 19 41–6

- [12] Lindemann F A 1910 The calculation of molecular vibration frequencies Z. Phys. 11 609–12
- [13] Plimpton S 1995 Fast parallel algorithms for short-range molecular dynamics *J. Comput. Phys.* **117** 1–19
- [14] Williams P L, Mishin Y and Hamilton J C 2006 An embedded-atom potential for the Cu–Ag system Modelling Simul. Mater. Sci. Eng. 14 817–33
- [15] Mishin Y 2006 EAM potential for Ag Retrieved from https://ctcms.nist.gov/potentials/Download/ 2006--Williams-P-L-Mishin-Y-Hamilton-J-C--Ag/2/Ag.eam.alloy (accessed on 10 August 2021)
- [16] Shinoda W, Shiga M and Mikami M 2004 Rapid estimation of elastic constants by molecular dynamics simulation under constant stress Phys. Rev. B 69 134103
- [17] Stukowski A 2009 Visualization and analysis of atomistic simulation data with OVITO-the Open Visualization Tool Modelling Simul. Mater. Sci. Eng. 18 015012
- [18] Larsen P M, Schmidt S and Schiøtz J 2016 Robust structural identification via polyhedral template matching Modelling Simul. Mater. Sci. Eng. 24 055007
- [19] Hull D and Bacon D J 2011 Introduction to Dislocations (Oxford: Heinemann)
- [20] Briggs R et al 2019 Measurement of body-centered cubic gold and melting under shock compression Phys. Rev. Lett. 123 045701
- [21] Xiong Q-l, Kitamura T and Li Z 2019 Transient phase transitions in single-crystal coppers under ultrafast lasers induced shock compression: a molecular dynamics study J. Appl. Phys. 125 194302
- [22] Stukowski A, Bulatov V V and Arsenlis A 2012 Automated identification and indexing of dislocations in crystal interfaces Modelling Simul. Mater. Sci. Eng. 20 085007
- [23] Chitrakar T V, Keto J W, Becker M F and Kovar D 2017 Particle deposition and deformation from high speed impaction of Ag nanoparticles Acta Mater. 135 252–62
- [24] Chitrakar T V, Noiseau G J J, Keto J W, Becker M F and Kovar D 2019 An experimental and computational study of high speed two-particle impacts of Ag nanoparticles J. Appl. Phys. 125 195104